Annals of Biomedical Engineering, Vol. 35, No. 5, May 2007 (© 2007) pp. 711–723
DOI: 10.1007/s10439-007-9258-1

Modeling Plaque Fissuring and Dissection during Balloon Angioplasty Intervention

T. Christian Gasser[1] and Gerhard A. Holzapfel [1,2]

[1]Department of Solid Mechanics, School of Engineering Sciences, Royal Institute of Technology (KTH), Osquars Backe 1, SE-100 44, Stockholm, Sweden; and [2]Institute for Biomechanics, Center for Biomedical Engineering, Graz University of Technology, 8010 Graz, Austria

(Received 1 September 2006; accepted 9 January 2007; published online 24 March 2007)

Abstract—Balloon angioplasty intervention is traumatic to arterial tissue. Fracture mechanisms such as plaque fissuring and/or dissection occur and constitute major contributions to the lumen enlargement. However, these types of mechanically-based traumatization of arterial tissue are also contributing factors to both acute procedural complications and chronic restenosis of the treatment site. We propose physical and finite element models, which are generally useable to trace fissuring and/or dissection in atherosclerotic plaques during balloon angioplasty interventions. The arterial wall is described as an anisotropic, heterogeneous, highly deformable, nearly incompressible body, whereas tissue failure is captured by a strong discontinuity kinematics and a novel cohesive zone model. The numerical implementation is based on the partition of unity finite element method and the interface element method. The later is used to link together meshes of the different tissue components. The balloon angioplasty-based failure mechanisms are numerically studied in 3D by means of an atherosclerotic-prone human external iliac artery, with a type V lesion. Image-based 3D geometry is generated and tissue-specific material properties are considered. Numerical results show that in a primary phase the plaque fissures at both shoulders of the fibrous cap and stops at the lamina elastica interna. In a secondary phase, local dissections between the intima and the media develop at the fibrous cap location with the smallest thickness. The predicted results indicate that plaque fissuring and dissection cause localized mechanical trauma, but prevent the main portion of the stenosis from high stress, and hence from continuous tissue damage.

Keywords—Artery, Atherosclerotic plaque, Balloon angioplasty, Cohesive zone model, Dissection, FEM, Plaque fissuring.

INTRODUCTION

Arterial dissections may occur spontaneously or traumatic and are frequently observed in clinical practice. In particular, the fracture mechanism occurring during balloon angioplasty,[41] which to model is one focus of the present work, is fundamentally traumatic to arterial tissue.[6,61] Balloon angioplasty involves denudation of the endothelium, disruption of the intima and the atherosclerotic plaque with frequent separation from or dissection of the media, and overstretching of remnant non-diseased tissue in lesions (see Humphrey[37] and references therein). Plaque fissuring and/or local dissection (probably secondary to plaque fissuring) are particular forms of balloon angioplasty-induced arterial trauma involving laceration and/or cleavage of the arterial wall.[9,41,47] Angioplasty-induced dissections have been implicated as a contributing factor to both acute procedural complications (abrupt re-closure, ischemia, myocardial infarction, emergency surgery and coronary micro-embolization[1,10,11,36,55]) and chronic restenosis of the treatment site.[38]

Although arterial dissection is a frequently occurring phenomenon and a challenging clinical entity, the underlying biomechanics remains largely unclear. Only a few studies investigate the underlying biomechanics of failure initiation and propagation in atherosclerotic plaques. For experimental studies see the reviews on the biomechanics of atherosclerotic tissues and plaque rupture by Richardson[50,51] and Salunke and Topoleski,[56] and the literature survey on failure properties of the aorta by Sommer *et al.*[58] In the later experimental study[58] also dissection properties of the human aortic media are documented allowing the development of suitable constitutive models. It seems that only one computational model is yet available in the literature that allows the study of failure propagation in arterial tissue caused by balloon angioplasty.[16] Computational models are best suited to uncover the mechanisms of arterial failure, and hence helpful to optimize balloon angioplasty interventions.

Besides three-dimensional morphological data, the constitutive response of the involved tissue

Address correspondence to Gerhard A. Holzapfel, Department of Solid Mechanics, School of Engineering Sciences, Royal Institute of Technology (KTH), Osquars Backe 1, SE-100 44, Stockholm, Sweden. Electronic mail: gh@hallf.kth.se

components is of fundamental importance in order to reliably predict the evolutions of tissue stresses and strains during balloon angioplasty. The (rubber-like) non-collagenous matrix, the (leather-like) collagen fibers, and the smooth muscle cells control the mechanical properties of arterial walls. In particular, in the media of elastic arteries these three components are present in the medial lamellar units,[7,65] each of which is about 10 μm thick.[49] The highly organized structure of the arterial wall[49] causes its local cylindrical orthotropy,[46,64,67] and, in particular, its laminated structures are prone to split by creating a cleavage plane between adjacent lamellae.

The present work aims to model fissuring of tissue components, and dissection from each other typically occurring during balloon angioplasty intervention. We pursue the strong discontinuity approach, and model a material surface separation by a jump in the displacement field. We postulate the existence of a fracture process zone and regard plaque fissuring and dissection as a gradual process in which separation between material surfaces is resisted by a cohesive traction. In particular, recent histological investigations[58] highlight that (collagen and elastin) fiber bridging might play a dominant role in arterial dissection, which motivates to use this approach rather than the theory of sharp crack tips. We employ a (discrete) constitutive description of the cohesive zone, which is based on an isotropic traction separation law with isotropic damage.

The proposed computational 3D failure model combines the cohesive zone representation of failure with the partition of unity finite element method (PUFEM) and the interface element method (IEM). In particular, IEM is applied to interfaces with non-matching nodes allowing the discretization of the involved tissue components independently from each other and to link them together. The proposed numerical concept is based on a consistent linearization of the underlying variational formulation which serves as a basis for an effective and robust numerical description of failure propagation in arterial tissue. The balloon angioplasty-based failure mechanism is numerically studied by means of an atherosclerotic-prone human external iliac artery. The considered region of the atherosclerotic lesion is of type V according to the histological classification of Stary.[59] The model's geometry was generated from high-resolution magnetic resonance imaging (hrMRI) data, and the tissue-specific material, structural and cohesive parameters were considered. The balloon angioplasty intervention is numerically performed by solving the balloon/artery interaction as a 3D contact problem. Novel results on plaque fissuring, tissue dissection and on the stress distribution in the individual tissue components occurring during balloon dilatation of this specific atherosclerotic lesion are discussed in detail, and possible consequences are deduced.

MODELING ASSUMPTIONS

In this section the modeling assumptions are briefly described. In particular the underlying continuum mechanical basis and the proposed finite element implementation are discussed to some extent. An artery, when expanded during balloon angioplasty, is subject to (quasi-static) mechanical loads which are much higher than the loads under physiological conditions. Hence, it is justified to neglect all dynamic effects inherent to the cardiovascular system so that we pursue a quasi-static approach herein. A comprehensive introduction and derivation of the underlying framework is provided by Gasser and Holzapfel.[19]

Continuum Mechanical Basis

Strong Discontinuity Kinematics

We pursue the strong discontinuity approach in which the discontinuity in the displacement field describes tissue failure, i.e. fissuring and/or dissection. We assume that a discontinuity $\partial\Omega_{0\mathrm{d}}$ separates a body Ω_0 into two sub-bodies, which themselves occupy the sub-domains Ω_{0+} and Ω_{0-}, so that $\partial\Omega_{0\mathrm{d}} \cap \Omega_{0+} > \cap\Omega_{0-} = \emptyset$ and $\Omega_{0+} \cup \partial\Omega_{0\mathrm{d}} \cup \Omega_{0-} = \Omega_0$. Here we denote elements in the reference configuration by the subindex 0. For simplicity, a single discontinuity is assumed to describe the underlying kinematics. However, note that according to the numerical schemas described below, we can handle multiple discontinuities, and also interactions between tissue fissuring and dissection.

A deformation $\boldsymbol{\chi}(\mathbf{X})$, applied to the reference configuration, maps Ω_{0+} and Ω_{0-} into their current configurations Ω_+ and Ω_-, where $\mathbf{X}$ denotes the referential position of a material point. Consequently, the displacement at $\mathbf{X}$ is assumed to be $\mathbf{u}(\mathbf{X}) = \mathbf{u}_{\mathrm{c}}(\mathbf{X}) + \mathscr{H}(\mathbf{X})\mathbf{u}_{\mathrm{e}}(\mathbf{X})$, where $\mathbf{u}_{\mathrm{c}}$ and $\mathbf{u}_{\mathrm{e}}$ are regular and enhanced displacement fields, respectively.[2,44] Here $\mathscr{H}(\mathbf{X})$ denotes the *Heaviside* function with the values 0 and 1 for $\mathbf{X} \in \Omega_{0-}$ and $\mathbf{X} \in \Omega_{0+}$, respectively. In addition, we introduce the unit normal vector $\mathbf{N}(\mathbf{X})$, which yields the orientation of $\partial\Omega_{0\mathrm{d}}$ in $\mathbf{X}$, see Fig. 1.

Standard derivation[24,43] and the use of the property $\mathrm{Grad}\mathscr{H}(\mathbf{X}) = \delta_{\mathrm{d}}\mathbf{N}(\mathbf{X}_{\mathrm{d}})$ defines the corresponding deformation gradient

$$\mathbf{F}(\mathbf{X}) = \mathbf{I} + \mathrm{Grad}\ \mathbf{u}(\mathbf{X}) = \mathbf{I} + \mathrm{Grad}\ \mathbf{u}_{\mathrm{c}}(\mathbf{X}) + \mathscr{H}\mathrm{Grad}\ \mathbf{u}_{\mathrm{e}}(\mathbf{X}) + \delta_{\mathrm{d}}(\mathbf{X})\mathbf{u}_{\mathrm{e}}(\mathbf{X}) \otimes \mathbf{N}(\mathbf{X}_{\mathrm{d}}), \quad (1)$$

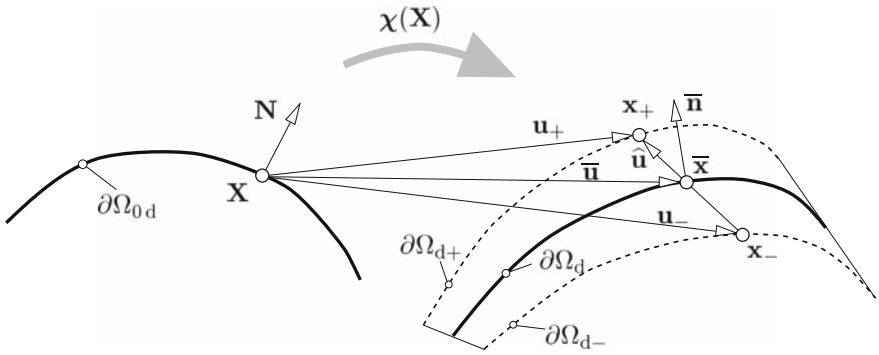

FIGURE 1. Strong discontinuity kinematics.

which serves as the basic expression for the right and left Cauchy-Green tensors, $\mathbf{C} = \mathbf{F}^{\mathrm{T}}\mathbf{F}$ and $\mathbf{b} = \mathbf{F}\mathbf{F}^{\mathrm{T}}$, respectively. Here $\mathbf{I}$ denotes the identity tensor and the material gradient operator is defined by $\mathrm{Grad}(\bullet) = \partial(\bullet)/\partial\mathbf{X}$. In addition, δ_{d} denotes the *Dirac-delta* functional with $\delta_{\mathrm{d}} = 0$ and $\delta_{\mathrm{d}} \to \infty$ for $\mathbf{X} \notin \partial\Omega_{0\mathrm{d}}$ and $\mathbf{X} \in \partial\Omega_{0\mathrm{d}}$, respectively.

In order to provide a discrete constitutive description of the cohesive traction acting at the displacement discontinuity, we introduce the gap displacement $\widehat{\mathbf{u}}(\mathbf{X})$ and the average displacement $\overline{\mathbf{u}}(\mathbf{X})$ related to a point $\overline{\mathbf{x}}$ located at the fictitious spatial discontinuity $\partial\Omega_{\mathrm{d}}$, see Fig. 1. The spatial orientation of $\partial\Omega_{\mathrm{d}}$ in $\overline{\mathbf{x}}$ is defined by the unit normal vector $\overline{\mathbf{n}}$ which can be interpreted as a weighted push-forward operation of the covariant vector $\mathbf{N}$. The fictitious spatial discontinuity $\partial\Omega_{\mathrm{d}}$ is assumed to be in the middle between the two physical surfaces $\partial\Omega_{\mathrm{d}+}$ and $\partial\Omega_{\mathrm{d}-}$, which originate from $\partial\Omega_{0\mathrm{d}}$.

According to the introduced kinematics, a referential point $\mathbf{X}$ maps into the two spatial points $\mathbf{x}_+$ and $\mathbf{x}_-$, which uniquely defines the gap and average displacements of the discontinuity, i.e. $\widehat{\mathbf{u}} = \mathbf{x}_+ - \mathbf{x}_-$ and $\overline{\mathbf{u}} = (\mathbf{x}_+ + \mathbf{x}_-)/2$, see Fig. 1.

Variational Formulation

The variational formulation for a quasi-static finite element model is based on a single-field variational principle,[24] i.e. $\int_{\Omega_0} \mathrm{Grad}\,\delta\mathbf{u} : \mathbf{P}(\mathbf{F})\mathrm{d}V - \delta\Pi^{\mathrm{ext}}(\delta\mathbf{u}) = 0$, where $\mathbf{P}(\mathbf{F})$ and $\delta\mathbf{u}$ denote the first Piola-Kirchhoff stress tensor and the admissible variation of the displacement field $\mathbf{u}$, respectively. The integration is taken over the reference configuration Ω_0, where $\mathrm{d}V$ denotes the referential volume element. In addition, the contributions due to external loading are summarized in the virtual external potential energy $\delta\Pi^{\mathrm{ext}}$. We assume that loads do not depend on the deformation of the body.

According to the introduced displacement field its admissible variation reads $\delta\mathbf{u} = \delta\mathbf{u}_{\mathrm{c}} + \mathscr{H}\delta\mathbf{u}_{\mathrm{e}}$, and after some algebraic manipulations, we get the two spatial variational statements[15]

$$\left.\begin{aligned} &\int_{\Omega_-} \mathrm{sym}(\mathrm{grad}_{\mathrm{c}}\delta\mathbf{u}_{\mathrm{c}}) : \boldsymbol{\sigma}_{\mathrm{c}}\mathrm{d}v \\ &\qquad + \int_{\Omega_+} \mathrm{sym}(\mathrm{grad}_{\mathrm{e}}\delta\mathbf{u}_{\mathrm{c}}) : \boldsymbol{\sigma}_{\mathrm{e}}\mathrm{d}v - \delta\Pi_{\mathrm{c}}^{\mathrm{ext}}(\delta\mathbf{u}_{\mathrm{c}}) = 0, \\ &\int_{\Omega_+} \mathrm{sym}(\mathrm{grad}_{\mathrm{e}}\delta\mathbf{u}_{\mathrm{e}}) : \boldsymbol{\sigma}_{\mathrm{e}}\mathrm{d}v \\ &\qquad + \int_{\partial\Omega_{\mathrm{d}}} \mathbf{t}\cdot\delta\mathbf{u}_{\mathrm{e}}\mathrm{d}s - \delta\Pi_{\mathrm{e}}^{\mathrm{ext}}(\delta\mathbf{u}_{\mathrm{e}}) = 0, \end{aligned}\right\} \quad (2)$$

where $\delta\Pi_{\mathrm{c}}{}^{\mathrm{ext}}$ and $\delta\Pi_{\mathrm{e}}{}^{\mathrm{ext}}$ are external contributions which refer to the domains Ω_{0-} and Ω_{0+}, respectively. In addition, $\mathrm{d}v$ and $\mathrm{d}s$ are the spatial volume and surface elements, respectively.

Here, $\boldsymbol{\sigma}_{\mathrm{c}} = J_{\mathrm{c}}^{-1}\mathbf{P}(\mathbf{F}_{\mathrm{c}})\mathbf{F}_{\mathrm{c}}^{\mathrm{T}}$ and $\boldsymbol{\sigma}_{\mathrm{e}} = J_{\mathrm{e}}^{-1}\mathbf{P}(\mathbf{F}_{\mathrm{e}})\mathbf{F}_{\mathrm{e}}^{\mathrm{T}}$ denote the Cauchy stress tensors and $\mathbf{t} = \mathbf{T}\mathrm{d}S/\mathrm{d}s$ is the Cauchy traction vector associated with a fictitious discontinuity $\partial\Omega_{\mathrm{d}}$, while $\mathbf{T}$ is the first Piola-Kirchhoff traction vector associated with the related fictitious discontinuity $\partial\Omega_{0\mathrm{d}}$. The spatial gradients in (2) are defined according to $\mathrm{grad}_{\mathrm{c}}(\bullet) = \mathrm{Grad}(\bullet)\mathbf{F}_{\mathrm{c}}^{-1}$, $\mathrm{grad}_{\mathrm{e}}(\bullet) = \mathrm{Grad}(\bullet)\mathbf{F}_{\mathrm{e}}{}^{-1}$, and $\mathrm{sym}(\bullet) = ((\bullet) + (\bullet)^{\mathrm{T}})/2$ furnishes the symmetric part of $(\bullet)$. For a consistent linearization of the statements (2), we refer to Gasser and Holzapfel,[15] and references therein.

Interface Representation of the Discontinuity

It is convenient to focus here on the referential variational formulation, which, for a quasi-static interface element model, is based on the single-field variational principle[45] $\delta\Pi = \int_{\partial\Omega_{0\mathrm{d}}} \mathbf{T}\cdot\delta\widehat{\mathbf{u}}\mathrm{d}S = 0$. We assume now that[19] $\mathbf{T} = \mathbf{T}[\widehat{\mathbf{u}}(\overline{\mathbf{x}}), \overline{\mathbf{n}}(\widehat{\mathbf{u}}(\overline{\mathbf{x}})), \delta]$, and, therefore, $\mathbf{T}$ depends on the gap displacement $\widehat{\mathbf{u}}$, the unit normal vector $\overline{\mathbf{n}}$ onto the fictitious discontinuity $\partial\Omega_{0\mathrm{d}}$, and $\delta \in [0, \infty]$ which denotes an internal damage variable recording the history of the failure process. By neglecting external loading on the interface the consistent linearization of the traction term gives

$$\Delta\delta\Pi = \int_{\partial\Omega_{0\mathrm{d}}} \delta\widehat{\mathbf{u}} \cdot \mathbf{C}_{\widehat{\mathbf{u}}}\Delta_{\widehat{\mathbf{u}}}\mathrm{d}S + \int_{\partial\Omega_{0\mathrm{d}}} \delta\widehat{\mathbf{u}} \cdot \mathbf{C}_{\overline{\mathbf{n}}}\Delta_{\overline{\mathbf{u}}}\overline{\mathbf{n}}\mathrm{d}S + \int_{\partial\Omega_{0\mathrm{d}}} \delta\widehat{\mathbf{u}} \cdot \mathbf{C}_{\delta}\Delta_{\widehat{\mathbf{u}}}\delta\mathrm{d}S, \tag{3}$$

where $\mathbf{C}_{\widehat{\mathbf{u}}} = \partial\mathbf{T}/\partial\widehat{\mathbf{u}}, \mathbf{C}_{\overline{\mathbf{n}}} = \partial\mathbf{T}/\partial\overline{\mathbf{n}}, \mathbf{C}_{\delta} = \partial\mathbf{T}/\partial\delta$ describe the stiffness of the cohesive zone with respect to the gap displacement, the rotation and the growing damage. The notation $\Delta_a(\bullet)$ indicates the Gâteaux derivative of $(\bullet)$ in the direction of a, which is explained in more detail by Gasser and Holzapfel[15] and Holzapfel.[24]

Constitutive Formulation

In order to work with the above introduced variational statements, we have to provide continuous and discontinuous constitutive formulations to describe the bulk and the cohesive material responses. We assume both constitutive formulations to be independent from each other.

We start with the bulk constitutive model, and review that the arterial wall is anisotropic, heterogeneous, highly deformable, nearly incompressible and shows pseudo-elastic behavior.[20,27,29,37] In the present work, the complex architecture of an arterial layer is represented mechanically as a fiber-reinforced composite,[25,27] in which two families of collagen fibers are embedded in an isotropic groundmatrix. In addition, the dispersion of the collagen fiber orientation, as pointed out in, e.g., Finlay *et al.*,[12] is also represented.[20] In particular, we introduce (symmetric) generalized structure tensors, defined by $\mathbf{H}_i = \frac{1}{4\pi}\int_{\omega}\rho(\mathbf{M})\,\mathbf{M}\otimes\mathbf{M}\mathrm{d}\omega$, which serve as a continuum representation of dispersed fiber orientations within the ith family of collagen fibers. Here $\rho(\mathbf{M})$ denotes the normalized density function of the referential orientation $\mathbf{M}$, $|\mathbf{M}| = 1$, and $\mathrm{d}\omega = \sin\Theta\mathrm{d}\Theta\mathrm{d}\Phi$ is the unit sphere with the two Eulerian angles $\Theta \in [0,\pi]$ and $\Phi \in [0,2\pi]$.

Based on experimental quantifications of collagen formation in arterial layers,[12] we assume a transversely isotropic distribution of the collagen within a particular fiber family such that

$$\mathbf{H}_i = \kappa\mathbf{I} + (1-3\kappa)\mathbf{a}_{0i}\otimes\mathbf{a}_{0i}, \quad \kappa = \frac{1}{4}\int_0^{\pi}\rho(\Theta)\sin^3\Theta\mathrm{d}\Theta \tag{4}$$

hold. Here, $\mathbf{a}_{0i}$ denotes the (mean) preferred direction of the collagen, whereas κ characterizes the related dispersion around $\mathbf{a}_{0i}$.[20]

According to Holzapfel and Weizsäcker[35] we assume an additive decomposition of the strain-energy function. In addition, we propose that the isochoric strain energy $\overline{\Psi}$ stored in the non-collagenous and collagenous components is according to $\overline{\Psi}(\overline{\mathbf{C}},\mathbf{H}_i) = \overline{\Psi}_{\mathrm{g}}(\overline{\mathbf{C}}) + \sum_{i=1,2}\overline{\Psi}_{\mathrm{f}i}(\overline{\mathbf{C}},\mathbf{H}_i(\mathbf{a}_{0i},\kappa))$, where $\overline{\mathbf{C}}$ denotes the modified right Cauchy-Green tensor.[24] While the non-collagenous contribution is modeled by the neo-Hookean strain-energy function $\overline{\Psi}_{\mathrm{g}}(\overline{\mathbf{C}}) = \mu(\mathrm{tr}\overline{\mathbf{C}} - 3)/2$, the strain energy stored in the collagen fibers is proposed to be captured by the function[20]

$$\overline{\Psi}_{\mathrm{f}i}(\overline{\mathbf{C}},\mathbf{H}_i) = \frac{k_1}{2k_2}\{\exp[k_2\overline{E}_i{}^2] - 1\}, \qquad \overline{E}_i = \mathbf{H}_i : \overline{\mathbf{C}} - \mathbf{H}_i : \mathbf{I}, \quad i = 1,2, \tag{5}$$

where $\mathbf{H}_i : \overline{\mathbf{C}}$ denotes an invariant of the symmetric generalized structure tensors $\mathbf{H}_i$, and the symmetric tensor $\overline{\mathbf{C}}$. Consequently, the set (μ,k_1,k_2) of the material parameters needs to be quantified from experimental data, while the set $(\mathbf{a}_{0i},\kappa)$ of the structure parameters is characterized by the histology of the related tissue component.

We proceed now by describing the cohesive constitutive model. The complex irreversible changes in the microstructure of the individual tissue components due to, e.g., fissuring and dissection are lumped into a (discrete) cohesive zone, which is mechanically defined by the cohesive potential ψ. A justification for the application of the theory of cohesive zones rather than assuming sharp crack tips is mainly motivated by the (collagen and elastin) fiber cross-bridging, as can be seen through histological images.[58]

Within the present work we employ an isotropic cohesive model similar to the Rose, Smith and Ferrante universal binding law,[53,54] and used in the recent work by Gasser and Holzapfel,[19] namely

$$\psi(i_1,\delta) = \frac{c}{2}\exp(-a\delta)i_1, \tag{6}$$

where $i_1 = \widehat{\mathbf{u}}\cdot\widehat{\mathbf{u}}$ is the first invariant of the symmetric tensor $\widehat{\mathbf{u}}\otimes\widehat{\mathbf{u}}$ and the non-negative parameters a,c and δ characterize the traction separation properties of the cohesive zone. In particular, $\delta \in [0,\infty]$ denotes an internal damage variable. The term $\exp(-a\delta)$ is equivalent to $(1-d)$ known as the reduction factor from the isotropic continuum damage theory, where the damage variable $d \in [0,1]$ is the ratio between the damaged and the initial cross sectional areas of a material point.[24,39] With standard arguments, the Coleman-Noll procedure[8] implies the physical expression

$$\mathbf{T} = \frac{\partial\psi}{\partial\widehat{\mathbf{u}}} = c\exp(-a\delta)\widehat{\mathbf{u}} \tag{7}$$

for the first Piola-Kirchhoff traction vector $\mathbf{T}$. From (7) it is clear that c has the meaning of the initial stiffness of the cohesive zone.

Moreover, with the introduction of the mode I fracture energy, denoted by $\mathscr{G}_I$, as $\mathscr{G}_I = \int_0^\infty \mathbf{T}\cdot \mathrm{d}\widehat{\mathbf{u}} = \int_0^\infty c\exp(-a\delta)\widehat{u}\mathrm{d}\widehat{u} = c/a^2$, and the cohesive tensile strength T_0, which is the maximum traction obtained from model (7) to be $T_0 = c\exp(-1)/a$, we may deduce the useful relations

$$c = \frac{T_0^2\exp(2)}{\mathscr{G}_I}, \quad a = \frac{T_0\exp(1)}{\mathscr{G}_I} \tag{8}$$

for the introduced material parameters c and a, respectively. Finally, in order to complete the cohesive description, a damage surface $\phi(\widehat{\mathbf{u}},\delta) = |\widehat{\mathbf{u}}| - \delta = 0$ in the 3D gap displacement space is introduced, and it is assumed that $\dot{\delta} = \dot{\overline{|\widehat{\mathbf{u}}|}}$ captures the evolution of the internal (damage) variable δ.

The proposed model has the main advantage of a smooth transition from the stiffening into the softening branch (continuous envelope) of the cohesive zone, which is particularly helpful for dynamical computations. However, the capability of the cohesive model to fit experimental data is limited, e.g., relation $(8)_1$ indicates that a large fracture energy causes a low initial stiffness, which might not always meet experimental observations. The introduction of an additional material parameter, as shown by Gasser and Holzapfel,[14] can, to some extend, circumvent this drawback.

Finally, the penalty constraint $\psi_{\mathrm{pen}} = c_{\mathrm{pen}}\langle\widehat{\mathbf{u}}\cdot\overline{\mathbf{n}}\rangle^2/2$ against penetration is added to the cohesive potential (6), where $\langle(\bullet)\rangle = [(\bullet) + |(\bullet)|]/2$, defines the Macauley bracket function, while c_{pen} is a non-negative penalty parameter. The penalty formulation is exact when $c_{\mathrm{pen}} \to \infty$. This approach is suitable as long as small sliding of the interface is present, however, for large sliding the term needs to be replaced by a standard contact formulation.[66]

Finite Element Implementation

We restricted our finite element model in the sense that dissection type of failure can only propagate along interfaces between the different arterial layers, e.g., along the lamina elastica interna and externa. In contrast, tissue fissuring is under no such restriction; it is solely driven by the stress field. According to these assumptions, dissection failure is numerically represented by the IEM, while fissuring of layers is captured by the PUFEM. The two different numerical implementations, i.e. IEM and PUFEM of arterial failure, are discussed in the following.

Partition of Unity Finite Element Method (PUFEM)

According to the PUFEM, the displacement field $\underline{\mathbf{u}}$ is interpolated as

$$\underline{\mathbf{u}} = \sum_{I=1}^{n_{\mathrm{elem}}} N^I \underline{\mathbf{u}}_{I\mathrm{c}} + \mathscr{H}\sum_{I=1}^{n_{\mathrm{elem}}} N^I \underline{\mathbf{u}}_{I\mathrm{e}}, \tag{9}$$

where N^I are the standard (polynomial) shape functions, and I is an index running between 1 and the total number of finite element nodes, denoted by n_{elem}. Note that characters indicated by underlines denote the matrix notation of the associated tensor or vector (for example, $\underline{\mathbf{u}}$ is the matrix representation of vector $\mathbf{u}$). In (9), regular and enhanced nodal displacements are denoted by $\mathbf{u}_{I\,\mathrm{c}}$ and $\mathbf{u}_{I\,\mathrm{e}}$, respectively, and the Heaviside function $\mathscr{H}$ enriches (9) in order to achieve good local approximation properties.

Interpolation (9) in conjunction with the variational statements (2) render the following linearized algebraic set of equations for a particular finite element node I to[15]

$$\begin{bmatrix} \underline{\mathbf{K}}_{\mathbf{u}_\mathrm{c}\mathbf{u}_\mathrm{c}} & \underline{\mathbf{K}}_{\mathbf{u}_\mathrm{c}\mathbf{u}_\mathrm{e}} \\ \underline{\mathbf{K}}_{\mathbf{u}_\mathrm{e}\mathbf{u}_\mathrm{c}} & \underline{\mathbf{K}}_{\mathbf{u}_\mathrm{e}\mathbf{u}_\mathrm{e}} \end{bmatrix}_{i-1}^{I} \begin{bmatrix} \Delta\underline{\mathbf{u}}_\mathrm{c} \\ \Delta\underline{\mathbf{u}}_\mathrm{e} \end{bmatrix}_{i}^{I} = \begin{bmatrix} \underline{\mathbf{f}}_{\mathbf{u}_\mathrm{c}}^{\mathrm{ext}} \\ \underline{\mathbf{f}}_{\mathbf{u}_\mathrm{e}}^{\mathrm{ext}} \end{bmatrix}_{i-1}^{I} - \begin{bmatrix} \underline{\mathbf{f}}_{\mathbf{u}_\mathrm{c}}^{\mathrm{int}} \\ \underline{\mathbf{f}}_{\mathbf{u}_\mathrm{e}}^{\mathrm{int}} \end{bmatrix}_{i-1}^{I}, \tag{10}$$

where i, i–1 denote the iteration steps associated with a global Newton iteration, and $\Delta\underline{\mathbf{u}}_\mathrm{c}$ and $\Delta\underline{\mathbf{u}}_\mathrm{e}$ denote the increments of the regular and the enhanced nodal displacements, respectively.

In (10) the vectors $\underline{\mathbf{f}}_{\mathbf{u}_\mathrm{c}}^{\mathrm{ext}}$, $\underline{\mathbf{f}}_{\mathbf{u}_\mathrm{e}}^{\mathrm{ext}}$ and $\underline{\mathbf{f}}_{\mathbf{u}_\mathrm{c}}^{\mathrm{int}}$, $\underline{\mathbf{f}}_{\mathbf{u}_\mathrm{e}}^{\mathrm{int}}$ denote the external and internal nodal force vectors, respectively. For a detailed derivation of these vectors, and the contribution of the sub-matrices $\underline{\mathbf{K}}_{(\bullet\bullet)}$ (with the abbreviation $(\bullet\bullet)$ standing for $\mathbf{u}_\mathrm{c}\mathbf{u}_\mathrm{c}$, $\mathbf{u}_\mathrm{c}\mathbf{u}_\mathrm{e}$, $\mathbf{u}_\mathrm{e}\mathbf{u}_\mathrm{c}$ or $\mathbf{u}_\mathrm{e}\mathbf{u}_\mathrm{e}$) to the nodal stiffness matrix, as introduced in (10).[19] Finally, we emphasize that the cohesive traction $\mathbf{T}$ causes an off-diagonal contribution $\underline{\mathbf{K}}_{\mathbf{u}_\mathrm{c}\mathbf{u}_\mathrm{e}}$ and a diagonal contribution $\underline{\mathbf{K}}_{\mathbf{u}_\mathrm{e}\mathbf{u}_\mathrm{e}}$ to the element stiffness matrix.[14,15]

The proposed finite element model has been implemented into the multi-purpose finite element analysis program FEAP.[60] In addition, a separate package was developed to handle the geometrical representation and propagation of the developing cracks, which are utilized by the macro command language in FEAP after each load step.[18]

Interface Element Method (IEM)

In order to allow the generation of finite element meshes for the individual tissue geometries independent from each other, we use the IEM for non-matching nodes to link together the different three-dimensional geometries. Note that the considered IEM must handle the enhanced degrees of freedom used in PUFEM in

order to allow an interaction between the fissuring and dissection of the individual tissue layers.

Consequently, we introduce

$$\begin{aligned}\widehat{\underline{\mathbf{u}}} &= \sum_{I=1}^{n^{\text{if}}_{\text{elem}}} \widehat{N}_I \underline{\mathbf{u}}_{I\text{c}} + \mathscr{H} \sum_{I=1}^{n^{\text{if}}_{\text{elem}}} \widehat{N}_I \underline{\mathbf{u}}_{I\text{e}}, \\ \overline{\underline{\mathbf{u}}} &= \sum_{I=1}^{n^{\text{if}}_{\text{elem}}} \overline{N}_I \underline{\mathbf{u}}_{I\text{c}} + \mathscr{H} \sum_{I=1}^{n^{\text{if}}_{\text{elem}}} \overline{N}_I \underline{\mathbf{u}}_{I\text{e}},\end{aligned} \tag{11}$$

where $\widehat{\underline{\mathbf{u}}}$ and $\overline{\underline{\mathbf{u}}}$ denote the gap displacement and average displacement located at the fictitious spatial discontinuity, and $\widehat{N}_I$ and $\overline{N}_I$ are the interpolation functions associated with the Ith node, related to $\widehat{\underline{\mathbf{u}}}$ and $\overline{\underline{\mathbf{u}}}$, respectively. The index I in the sums of (11) runs between 1 and the total number of nodes of the interface element, denoted by $n^{\text{if}}_{\text{elem}}$.

According to relation (3), a straightforward algebraic manipulation gives the following linearized algebraic set of equations for a particular node I on the interface element

$$\begin{bmatrix} \underline{\mathbf{K}}^{\text{if}} & \underline{\mathbf{K}}^{\text{if}} \\ \underline{\mathbf{K}}^{\text{if}} & \underline{\mathbf{K}}^{\text{if}} \end{bmatrix}^{I}_{i-1} \begin{bmatrix} \Delta\underline{\mathbf{u}}_{\text{c}} \\ \Delta\underline{\mathbf{u}}_{\text{e}} \end{bmatrix}^{I}_{i} = - \begin{bmatrix} \underline{\mathbf{f}}^{\text{if}} \\ \underline{\mathbf{f}}^{\text{if}} \end{bmatrix}^{I}_{i-1}, \tag{12}$$

where i, $i-1$ denote the iteration steps associated with a global Newton iteration, and $\Delta\underline{\mathbf{u}}_{\text{c}}$, $\Delta\underline{\mathbf{u}}_{\text{e}}$ denote again the increments of the nodal displacements. The nodal force vector $\underline{\mathbf{f}}^{\text{if}}_I$ due to internal loading, and the stiffness sub-matrix $\underline{\mathbf{K}}^{\text{if}}_I$ of the Ith node are defined as

$$\begin{aligned}\underline{\mathbf{f}}^{\text{if}}_I = \int_{\partial\Omega^e_{0\text{d}}} \mathbf{T}\widehat{N}_I \,\mathrm{d}S, \quad \underline{\mathbf{K}}^{\text{if}}_I = \int_{\partial\Omega^e_{0\text{d}}} \widehat{N}_I \underline{\mathbf{C}}_{\widehat{\underline{\mathbf{u}}}} \widehat{N}_J \,\mathrm{d}S \\ - \int_{\partial\Omega^e_{0\text{d}}} \widehat{N}_I \underline{\mathbf{C}}_{\overline{\underline{\mathbf{n}}}} \overline{\underline{\mathbf{n}}} \,\mathrm{grad}\overline{N}^J \,\mathrm{d}S,\end{aligned} \tag{13}$$

respectively, where $\partial\Omega^e_{0\text{d}}$ denotes the discontinuity domain of the considered interface element in the reference configuration. It is important to note that in the case that the enhanced degrees of freedoms are active, the nodal stiffness in (12) becomes rank deficient, and hence the interface formulation can only be used in combination with the partition of unity (PU) finite elements.

The particular IEM with the related model has been realized by linking together two triangular facets. Hence, the interface element has 6 nodes, and it has been implemented into FEAP by using the user-defined element routine.

BALLOON ANGIOPLASTY MODEL

In this section plaque fissuring and local dissection of the atherosclerotic plaque are studied in more detail, since this type of failure is frequently identified after balloon angioplasty, see, e.g., the study by Coulden *et al.*[9] In particular, we have chosen an atherosclerotic-prone human external iliac artery (65 years, female), see Fig. 2(a), from which the different tissue types were prepared and mechanically tested in axial and circumferential directions. For the related anamnesis and the mechanical data (uniaxial tensile stress-stretch responses and ultimate tensile stresses and stretches) of the different tissues, see Holzapfel *et al.*,[32] specimen I therein. In addition, the three-dimensional reconstruction of the most important tissue boundaries of this specific atherosclerotic artery is performed by means of hrMRI and a specifically developed software tool which is based on a deformable model. Details on the method, the reconstruction technique and the validation approach is provided in the recent work by Auer *et al.*[3] (for a longitudinal section see also Fig. 1 in Holzapfel *et al.*,[33] where the same atherosclerotic artery was used to analyze the changes in its mechanical environment during interaction with different stents). As can be seen from the segmented macroscopic view in Fig. 2(a), the artery consists of seven different tissue components represented by the borderlines[32] (A = adventitia, M-nos = non-diseased media, I-nos = non-diseased intima, I-fc = fibrous cap, I-fm = fibrous intima at the medial border, I-lp = lipid pool, M-f = fibrous (diseased) media). Based on the histological composition and structure this atherosclerotic lesion is of type V[59] (for a partitioning of the pathogenesis of atherosclerosis into different stages of plaque formation see Fig. I in Stary[59]). A type V lesion (fibroatheroma) contains mainly reparative smooth muscle cells and fibrous tissue and, additionally, two or more lipid pools of unequal size separated from each other by cells and fibrous tissue.

For our numerical investigation we have now discretized the different tissue components of this atherosclerotic lesion by means of tetrahedral finite elements. For simplicity, we combined M-nos and M-f to one tissue component, labeled as 'media', and I-nos, I-fc and I-fm to another tissue component, labeled as 'intima'. Subsequently, we associate the media with the material properties of the non-diseased media (M-nos), and the intima with the fibrous cap (I-fc). Finally, we consider just a slice of the atherosclerotic lesion assumed to be at rest and stress free in the unloaded (initial) configuration, and composed of four different tissue components, as can be seen in Fig. 2(b).

Definition of the Material Axis

In order to apply the anisotropic constitutive model, as proposed above, the (mean) preferred direction of the collagen $\mathbf{a}_{0i}$ and the related dispersion κ have to be

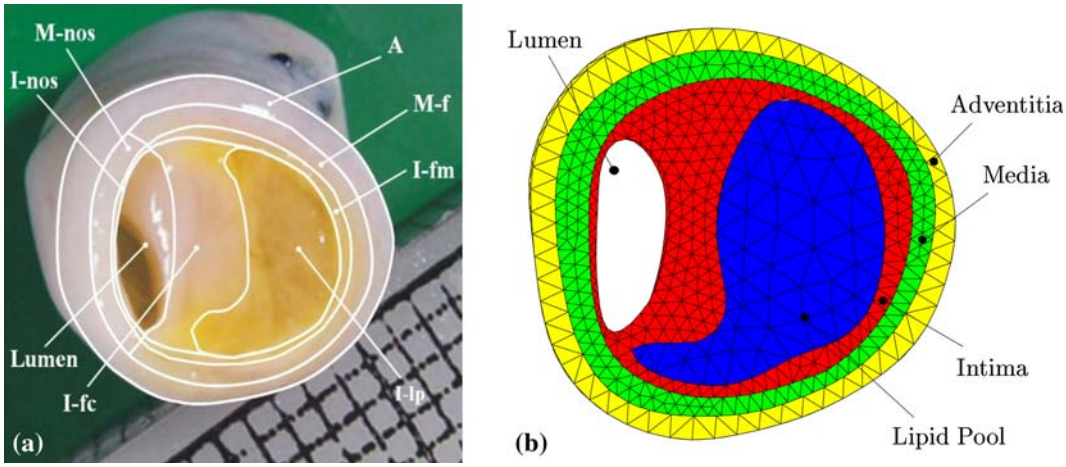

FIGURE 2. Human external iliac artery: (a) segmented macroscopic view of a type V lesion according to the histological classification of Stary[59] (adopted from Holzapfel *et al.*[32]). The borderlines represent the different tissue components. A = adventitia, M-nos = non-diseased media, I-nos = non-diseased intima, I-fc = fibrous cap, I-fm = fibrous intima at the medial border, I-lp = lipid pool, and M-f = fibrous (diseased) media); (b) 3D discretization of a slice of the atherosclerotic lesion composed of four different tissue components (labeled as adventitia, media, intima, lipid pool; for an explanation see the text) by means of tetrahedral finite elements. The individual tissues are meshed separately and linked together using the interface element method.

defined. For our analysis structural homogeneity is assumed, i.e. κ is constant and $\mathbf{a}_{0i}$ has the same components with respect to a local coordinate system (R, Θ, Z) within each tissue component (see Fig. 3). Apart from the histological quantification of $\mathbf{a}_{0\,i}$ and κ, the local coordinate system, i.e. the local material axes (R, Θ, Z), has to be defined in order to work with an anisotropic constitutive model.

Although diffusion MRI, which is based on the underlying water diffusion properties, is basically able to determine the microstructure of different atherosclerotic components,[62] this technique does not provide the resolution required for the present study. To overcome this shortcoming, we propose a novel theoretically-oriented method allowing the definition of a local coordinate system (R, Θ, Z) within all tissue components of the whole stenotic artery. The basic idea is to map the reference configuration Ω_0 of the artery to an eccentric thick-walled tube $\overline{\Omega}_0$, according to the deformation $\overline{\boldsymbol{\chi}}$ with $\overline{\mathbf{F}} = \partial\overline{\boldsymbol{\chi}}/\partial\mathbf{X}$, as can be seen in Fig. 3. Hence, in view of the simple geometry of $\overline{\Omega}_0$, the system $(\overline{\mathrm{R}}, \overline{\Theta}, \overline{\mathrm{Z}})$ located in $\overline{\Omega}_0$, i.e. the local radial $\overline{\mathbf{R}}$, the circumferential $\overline{\Theta}$ and the axial $\overline{\mathbf{Z}}$ directions, can then be defined in a straightforward way. Subsequently, a pull-back operation with the rotation tensor $\overline{\mathbf{Q}}(\bullet) = \overline{\mathbf{Q}}^{-1}(\bullet)$, with $(\bullet)$ denoting $(\mathbf{R}, \Theta, \mathbf{Z})$, defines the radial $\mathbf{R}$, circumferential Θ and axial $\mathbf{Z}$ directions in Ω_0, see Fig. 3. Here, the orthogonal tensor $\overline{\mathbf{Q}}$ is defined according to the multiplicative decomposition $\overline{\mathbf{F}} = \overline{\mathbf{Q}}\overline{\mathbf{U}}$, where $\overline{\mathbf{U}}$ denotes the right stretch tensor.[24] Note that the proposed method requires the definition of the configuration $\overline{\Omega}_0$, and this has some influence on the prediction of the material axes. In the current study, on a trial and error basis, we attempted to generate the eccentric thick-walled tube $\overline{\Omega}_0$ such that the deformation $\overline{\boldsymbol{\chi}}$ is minimized.

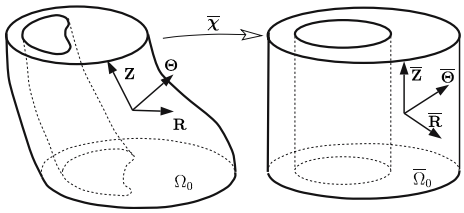

FIGURE 3. Transformation of the reference configuration Ω_0 of the stenotic artery to an eccentric thick-walled tube $\overline{\Omega}_0$.

Modeling Details

While we had access to reliable geometrical data of the involved tissue types, their structural quantification is partly based on assumptions. In particular, there are no data available in the literature regarding the (local) collagen structure of stenotic iliac arteries. However, structural data can, to some extend, be estimated from mechanical tests. To this end the structural parameters can be treated like material parameters and both

TABLE 1. Material and structural parameters describing the bulk material of the involved arterial tissue components (taken from Holzapfel *et al.*[30]).

Tissue	μ (kPa)	k_1 (kPa)	k_2 (-)	α (°)	κ (-)
Intima	78.9	23.7	26.3	0.0	0.0
Media	15.0	4.0	2.3	7.0	0.0
Adventitia	1.75	65.6	61.8	49.0	0.0
Lipid Pool	0.1	0.0	–	–	–

(structural and material) parameters can then be estimated from mechanical experiments. In the present analysis we adopted parameters defined in that way. They are provided by Holzapfel *et al.*[30] Note that the (mean) preferred direction $\mathbf{a}_{0i}$ of the collagen is assumed to have no radial component in the local coordinate system (R, Θ, Z) such that $\mathbf{a}_{0i}$ can uniquely be described by an angle α defined between the fiber reinforcement (orthotropy) and the circumferential direction Θ in the individual layers. The employed structural and material parameters of the involved arterial tissue components are summarized in Table 1.

Next, we quantify the failure properties of the individual tissue components. There are not much data available in the literature, and hence some estimations are required. The estimation of the tissue resistance to fissuring is based on the literature,[32,40,48] and on preliminary experiments performed in our own laboratory. Therefore, these data need to be seen as a rough estimation from available (published and unpublished) sources. In particular, no data are available to quantify the softening region, i.e. the fracture energy and/or the shape of the cohesive law for tissue fissuring. The dissection properties are based on recent experimental results obtained from peeling (healthy) aortic medias,[58] and these data aim to represent the cohesive properties of the lamina elastica interna (intima/media interface), and the lamina elastica externa (media/adventitia interface). The used cohesive parameters describing tissue fissuring and dissection are summarized in Table 2.

According to our experience, highly stenotic arteries show very little or no axial *in situ* pre-stress, i.e. the pre-stretch in the axial direction is approximately 1, which is not the case for healthy arteries. Hence, in order to account for this, we fixed the bottom and top faces of the analyzed slice in the axial direction. In addition, we neglected residual strains in the load-free configuration, and assumed the geometry shown in Fig. 2 to be stress free. The different tissue components were discretized separately using tetrahedral second-order finite elements and the mesh was generated with the software-package NETGEN.[57] Subsequently, the different meshes, with non-matching nodes at the interfaces, were linked together by using the IEM, as discussed in the previous section. A program that has been specifically developed is able to detect the different interfaces in an automatic way and provides the input data for FEAP.

TABLE 2. Cohesive parameters describing fissuring of and dissection from the involved arterial tissue components.

Cohesive zone	T_0 (kPa)	$\mathscr{G}_f$ (mJ)
Fissuring of the Intima	400.0	40
Fissuring of the Media	500.0	100
Fissuring of the Adventitia	2000.0	300
Lamina elastica interna (Intima/media dissection)	140.1	6.35
Lamina elastica externa (Media/adventitia dissection)	140.1	6.35
Intima/lipid pool interface	rigid	rigid

The values for T_0 and $\mathscr{G}_f$ are estimated from experimental tests.[32,40,48,58]

The mechanics of the balloon angioplasty intervention is modeled as a 3D contact problem, where the mechanical load caused by the balloon/artery contact finally leads to tissue failure. For simplicity we assumed the balloon to be a circular cylinder with continuously increasing diameter. This approach seems to capture the real situation at higher inflation pressure, which coincides with the loading state at which tissue failure is expected. Note that at lower inflation pressures a balloon of, e.g., the Grüntzig type, is not yet unfolded such that the pressure in the balloon acts directly on the artery, and hence a pressure-boundary condition seems to be more realistic. In our study we do not model the unfolding process of the balloon, which takes place at low inflation pressure at which complex (dynamic) unfolding effects might be present.

For the present computation a specifically developed automatic crack initialization algorithm captures the onset of tissue fissuring. To this end *crack root elements* are adopted for the case that the stress-based failure initialization criterion is met.[18] For algorithmic purposes we have to avoid that *crack root elements* are too close to existing tissue fissures. (For the case that *crack root elements* are initialized in a too narrow distance to existing cracks, the developing new crack might interact with the existing one, which cannot be handled by the current implementation.) In the present analysis we chose a minimum tolerable distance of $4.0\sqrt[3]{V_e}$, with V_e denoting the referential element volume.

Predicted Results

At the beginning of the computation, where the balloon/artery contact occurred, the 3D problem could not be solved in a quasi-static way. Therefore, to stabilize the scheme we added some numerical viscosity and solved the resulting first-order transient problem using the Newmark method provided by FEAP. The added viscosity was (very) small so that it did not affect the development of plaque fissuring and dissection in the atherosclerotic lesion, which occurs at a much higher load. After 132 load steps and a balloon diameter of $d_b = 4.42$ mm, the large mesh distortion in the lipid pool at the dissection site required a

termination of the computation. Re-meshing would have been required to overcome this drawback of the numerical model, which was not considered in the present study.

The deformed state of the stenosis at the maximum lumen diameter of $d_b = 4.42$ mm is shown in Fig. 4. For clarity the PU finite elements, which are those elements at which the failure criterion were met and discontinuities have been embedded, are removed. As can be seen from the results in Fig. 4, the plaque fissured at both shoulders of the intima, i.e. where the fibrous cap converts into the (healthy) intimal tissue. However, only at the side where the fibrous cap is thinner a pronounced cleavage of the arterial wall between the intima and the media developed, i.e. a dissection propagates along the lamina elastica interna. Interestingly, the tissue failure does not propagate into the lipid pool, which would lead to an extrusion of the lipid pool into the lumen, the typically observed type of revascularization during balloon angioplasty of fatty (yellow) plaques.[63] It needs to be emphasized, that, once developed, the tissue dissection propagates very much under mode I condition, and peeling seems to be the underlying dissection mechanism. Hence, in that sense the used cohesive material parameters, which were obtained from peeling experiments of human aortic medias,[58] are appropriate.

The predicted distributions of the maximum principal (Cauchy) stresses within the atherosclerotic lesion at balloon diameters $d_b = 3.52$ mm and 4.42 mm are illustrated in Fig. 5. The stresses are given in kPa and are shown for the intima, media and the adventitia. At the inflation state, corresponding to $d_b = 3.52$ mm, intimal fissuring starts at that side of the shoulder where the fibrous cap is thinner. As long as intact, the innermost layer of the lesion carries a significant part of the load. This load carrying mechanism is similar to that of an inflated thick-walled tube, where stress concentrations also occur at the inner wall. By tearing the intima and (partly) dissecting it from the media, a redistribution of the stresses occurs from the intima to the media, as clearly shown in Fig. 5. As expected, the stress in the adventitia increases during balloon inflation, however, the stress level remains relatively low, even behind the dissection. A possible explanation for the low stress level can be found in the intact media, which itself carries the main load. However, once the media gets more damaged a redistribution of the stress from the media to the adventitia will occur. Finally, the computational analysis shows that the lipid pool is under a small compressive hydrostatic stress (not shown in Fig. 5), which allows the extrusion of the fat into the lumen and a partial redistribution into the wall, as proposed by Toussaint *et al.*[63] for this type of lesion (here it is assumed that a channel between the lipid pool and the lumen exists). This mechanism is not considered in the present computation, but it contributes to the enlargement of the lumen of fatty (yellow) plaques.[63]

Surprisingly, after intimal fissuring occurs, the stress level in the overall tissue remains relatively moderate; it does not much exceed 300.0 kPa (apart from some small regions at the non-dissected shoulder of the intima). Hence, it is suggested that the propagation of the dissection effectively avoids stress-based damage in other regions of the lesion, as it has been confirmed by our previous work.[16]

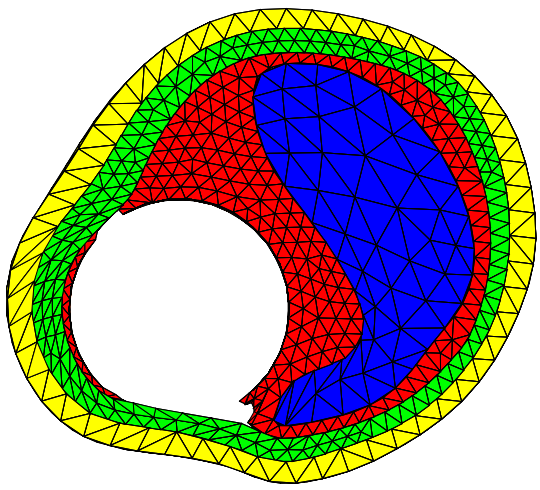

FIGURE 4. Deformed slice of the atherosclerotic lesion at a lumen diameter of $d_b = 4.42$ mm. Partition of unity finite elements are removed, for the sake of clarity.

CONCLUSION

Plaque fissuring and/or dissections of arterial tissue are frequently observed in clinical practice (see the reviews by Richardson[50,51]), and these types of failure mechanisms are known to be also caused during (balloon) angioplasty interventions.[9,41,47] Plaque fissuring and/or dissections represent major contributions to the lumen enlargement caused by balloon angioplasty.[41] Plaque fissuring and/or dissections have been shown to be an important predictor of the clinical outcome after balloon angioplasty intervention.[4,38] Interestingly, only a few studies investigate the underlying biomechanics of tissue failure in atherosclerotic plaques.

In the present work we proposed physical and finite element models in 3D, which are generally useable to trace fissuring and/or dissection in atherosclerotic plaques during balloon angioplasty interventions. The underlying continuum mechanical framework considered the atherosclerotic plaque as a

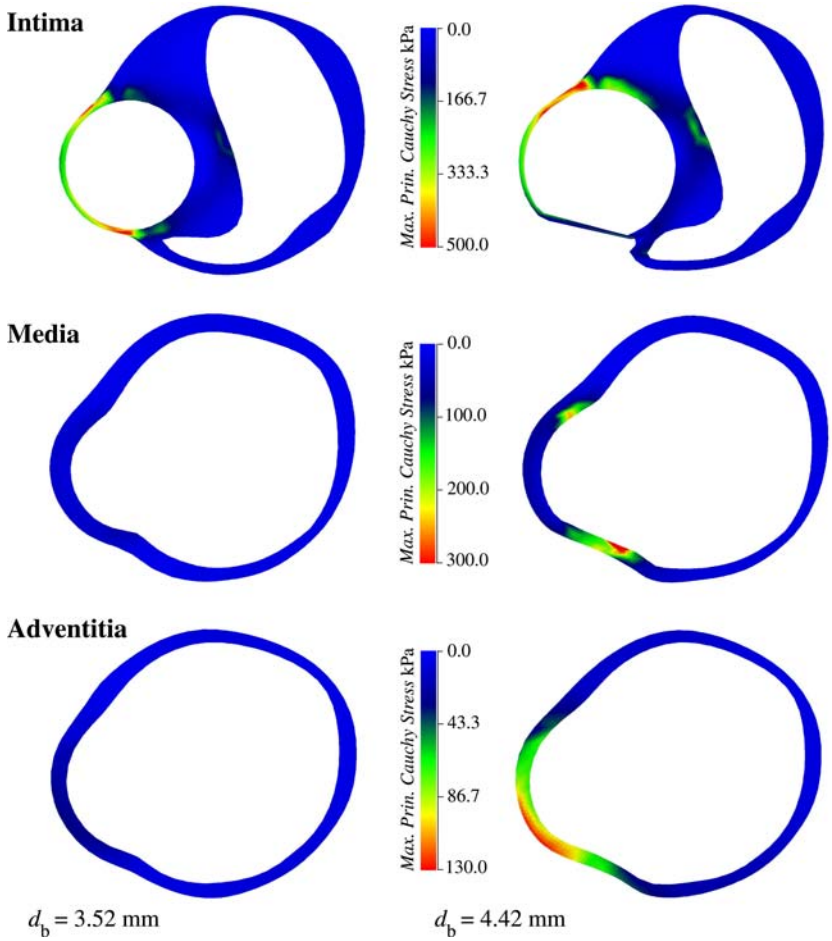

FIGURE 5. Distribution of maximum principal (Cauchy) stresses in the atherosclerotic lesion of a human external iliac artery during balloon angioplasty (type V lesion according to Stary[59]). Stresses are given for the intima, media and the adventitia at balloon diameters d_b = 3.52 mm and 4.42 mm.

highly deformable, locally anisotropic and heterogeneous body, which was assumed to be stress free in the unloaded (initial) configuration. Since the wall stresses due to artery (balloon) expansion are much higher than those due to physiological loading, we neglected dynamic effects inherent to the cardiovascular system, and claim that plaque fissuring and dissection caused during angioplasty intervention is most likely to be unaffected by blood-flow induced forces. Tissue failure was captured by means of the strong discontinuity kinematics, which characterize a material surface separation by a jump in the displacement field. Recent histological investigations[58] have highlighted the dominant role of (collagen and elastin) fiber bridging in arterial dissection, which was the motivation to use the theory of cohesive zones rather than the theory of sharp crack tips. The failure hypothesis of atherosclerotic plaques was numerically realized by means of PUFEM and IEM such that plaque fissuring and dissection, or a combination of them can be studied. Both numerical methods were based on a single-field variational formulation. The implementation of the related linearized problem represents a robust and efficient numerical basis for the study of the propagation of tissue failure in 3D. We modeled and investigated the evolution of plaque fissuring and dissection in an atherosclerotic-prone human external iliac artery (type V lesion according to Stary[59]) during balloon angioplasty intervention, for which the balloon/artery interaction was solved as a 3D contact problem. Finally, the lesion's geometry was reconstructed by means of hrMRI and a specifically developed software tool. Material, structural and cohesive parameters of the involved arterial tissue components were considered.

The performed 3D computations showed that in a primary phase the plaque fissured at both shoulders of the intima, and then stopped at the lamina elastica interna. In a secondary phase, local dissections between the intima and the media developed at the shoulder, where the fibrous cap is thinner. Interestingly, the dissection effectively reduced the stresses in

the stenosis and avoided continuous damage in the lesion. Hence, the mechanical trauma due to balloon angioplasty seems to remain localized at the dissection site rather than spread out all over the lesion.

The used numerical concept to describe tissue failure in a phenomenological way was based on cohesive zones, which is known to be the proper concept to handle strain softening problems. In particular, the numerical concept does not suffer from mesh-sensitivity inherent to several alternative numerical approaches.[15] However, a crucial requirement for obtaining mesh-independent results is that the finite element size needs to be smaller than the characteristic length of the cohesive zone, which can be estimated from the cohesive law.[22] Consequently, the tissue failure under consideration requires such a fine computational grid that a large-scale analysis would have been computationally very expensive. Certainly, h refinement at locations where dissection regions appear could significantly reduce the computational costs.

Within this work we assumed that the load-free configuration of the lesion was free of stress, which is most probably not the case. Residual stresses in the load-free configuration have a big influence on the local stress field, and a moderate on the global response of healthy arteries.[20,27,28] It needs to be emphasized that the complex geometry and heterogeneity of atherosclerotic arteries cause also complex three-dimensional residual stress fields,[31] which cannot easily be incorporated, e.g., by 'closing an opened-up configuration', as it is usually performed for healthy arteries.

Certain assumptions were required to provide material and structural parameters for the present analysis since there is (still) a considerable lack of comprehensive experimental data in the literature. Although a small number of studies document experimental data regarding ultimate tensile stresses and strains,[32,40] no data are known regarding the softening region (fracture energy and/or the shape of the cohesive law). Note that balloon angioplasty locally exceeds the deformation at which the maximum cohesive tensile strength occurs, and predictions then depend on the used data describing the softening regions.

A fundamental and in-depth understanding of failure mechanisms in soft biological tissues is still missing. While dissections of arterial tissues have been investigated in detail in previous works,[5,42,52,58] the failure mechanisms of plaque fissuring are unclear. Within this work we assumed a Rankine failure criterion, in which the occurring maximum principal stress was compared with the tissue-specific stress limit. However, recent failure studies indicated that shear stress in the non-collagenous matrix might trigger tissue failure.[21] To be more specific, pull-out and peeling of collagen fibers might be the dominate failure mechanism rather than rupture of collagen fibers. To some extend this observation has been justified by our experimental dissection studies.[58]

It is known that beyond a certain loading point, the arterial widening becomes permanent due to balloon-induced overstretching, see the related experimental seminal study on dilated cadaveric arteries by Castaneda-Zuniga *et al.*[6] In particular, during dilation remnant non-diseased tissues in lesions are loaded beyond the elastic (physiological) limit, and the overstretch contributes to the lumen enlargement, a mechanism suggested by Hjemdahl-Monsen *et al.*[23] Some of our earlier constitutive models[13] assumed tissue damage due to accumulation of plastic deformation in the non-collagenous matrix. Hence, permanent deformations of the tissue components and the associated changes of the mechanical environment during balloon angioplasty can be addressed.[17,26,30,34] It seems, however, that mainly fibrotic stenosis are effected by this mechanism.[63] Since we studied a lipid-filled plaque we have, consequently, neglected the inelastic effect due to permanent tissue deformation. Apart from all these limitations the proposed physical and numerical model should be regarded as a further step towards computational aided angioplasty.

ACKNOWLEDGMENTS

We would like to thank *Martin Auer* and *Dimitrios E. Kiousis* for their helpful support to generate the finite element grids. Financial support for this research was partly provided by the Austrian Science Foundation under START-Award Y74-TEC. This support is gratefully acknowledged.

REFERENCES

[1]Agarwal, R., U. Kaul, V. Dev, S. Sharma, and P. Venugopal. The morphology of coronary arterial dissection occurring subsequent to angioplasty and its influence on acute complications. *Int. J. Cardiol.* 31:59–64, 1991.

[2]Armero, F. and K. Garikipati. An analysis of strong discontinuities in multiplicative finite strain plasticity and their relation with the numerical simulation of strain localization in solids. *Int. J. Solids Struct.* 33:2863–2885, 1996.

[3]Auer, M., R. Stollberger, P. Regitnig, F. Ebner, and G. A. Holzapfel. 3-D reconstruction of tissue components for atherosclerotic human arteries based on high-resolution MRI. *IEEE Trans. Med. Imaging* 25:345–357, 2006.

[4]Black, A. J., D. L. Namay, A. L. Niederman, N. J. Lembo, G. S. Roubin, J. S. Douglas Jr., and S. B. King III. Tear or dissection after coronary angioplasty Morphologic correlates of an ischemic complication. *Circulation* 79:1035–1042, 1989.

[5]Carson, M. W. and M. R. Roach. The strength of the aortic media and its role in the propagation of aortic dissection. *J. Biomech.* 23:579–588, 1990.

[6]Castaneda-Zuniga, W. R., A. Formanek, M. Tadavarthy, Z. Vlodaver, J. E. Edwards, C. Zollikofer, and K. Amplatz. The mechanism of balloon angioplasty. *Radiology* 135:565–571, 1980.
[7]Clark, J. M. and S. Glagov. Transmural organization of the arterial media: The lamellar unit revisited. *Arteriosclerosis* 5:19–34, 1985.
[8]Coleman, B. D. and W. Noll. The thermodynamics of elastic materials with heat conduction and viscosity. *Arch. Rat. Mech. Anal.* 13:167–178, 1963.
[9]Coulden, R. A., H. Moss, M. J. Graves, D. J. Lomas, D. S. Appleton, and P. L. Weissberg. High resolution magnetic resonance imaging of atherosclerosis and the response to balloon angioplasty. *Heart* 83:188–191, 2000.
[10]Cripps, T. R., J. M. Morgan, and A. F. Rickards. Outcome of extensive coronary artery dissection during coronary angioplasty. *Br. Heart J.* 66:3–6, 1991.
[11]Detre, K. M., D. R. Holmes Jr., R. Holubkov, M. J. Cowley, M. G. Bourassa, D. P. Faxon, G. R. Dorros, L. G. Bentivoglio, K. M. Kent, and R. K. Myler. Incidence and consequences of periprocedural occlusion: The 1985-1986 National Heart, Lung, and Blood Institute Percutaneous Transluminal Coronary Angioplasty Registry. *Circulation* 82:739–750, 1990.
[12]Finlay, H. M., P. Whittaker, and P. B. Canham. Collagen organization in the branching region of human brain arteries. *Stroke* 29:1595–1601, 1998.
[13]Gasser, T. C. and G. A. Holzapfel. A rate-independent elastoplastic constitutive model for (biological) fiber-reinforced composites at finite strains: Continuum basis, algorithmic formulation and finite element implementation. *Comput. Mech.* 29:340–360, 2002.
[14]Gasser, T. C. and G. A. Holzapfel. Geometrically nonlinear and consistently linearized embedded strong discontinuity models for 3D problems with an application to the dissection analysis of soft biological tissues. *Comput. Methods Appl. Mech. Eng.* 192:5059–5098, 2003.
[15]Gasser, T. C. and G. A. Holzapfel. Modeling 3D crack propagation in unreinforced concrete using PUFEM. *Comput. Methods Appl. Mech. Eng.* 194:2859–2896, 2005.
[16]Gasser T. C. and G. A. Holzapfel. Physical and numerical modeling of dissection propagation in arteries caused by balloon angioplasty. In Hamza, M. H. (ed.) Proceedings of the 3rd IASTED International Conference on Biomechanics, Anaheim. ACTA Press, 2005, pp. 229–233.
[17]Gasser T. C. and G. A. Holzapfel. Finite element modeling of balloon angioplasty by considering overstretch of remnant non-diseased tissues in lesions. *Comput. Mech.*, 2006, online doi 10.1007/s00466-006-0081-6.
[18]Gasser, T. C. and G. A. Holzapfel. 3D crack propagation in unreinforced concrete. A two-step algorithm for tracking 3D crack paths. *Comput. Methods Appl. Mech. Eng.* 195:5198–5219, 2006.
[19]Gasser, T. C. and G. A. Holzapfel. Modeling the propagation of arterial dissection. *Eur. J. Mech. A/Solids* 25:617–633, 2006.
[20]Gasser, T. C., R. W. Ogden, and G. A. Holzapfel. Hyperelastic modelling of arterial layers with distributed collagen fibre orientations. *J. R. Soc. Interface* 3:15–35, 2006.
[21]Haslach, H. W. Rupture mechanisms in circulatory system vascular tissue. In Abstracts of the 5th World Congress of Biomechanics. Munich, Germany, 29 July–4 August 2006. Elsevier, 2006, p. 274.
[22]Hillerborg, A., M. Modeer, and P. E. Petersson. Analysis of crack formation and crack growth in concrete by means of fracture mechanics and finite elements. *Cement Concr. Res.* 6:773–782, 1976.
[23]Hjemdahl-Monsen, C. E., J. A. Ambrose, S. Borrico, M. Cohen, W. Sherman, D. Alexopoulos, R. Gorlin, and V. Fuster. Angiographic patterns if balloon inflation during percutaneous transluminal coronary angioplasty: Role of pressure-diameter curves in studying distensibility and elasticity of the stenotic lesion and the mechanism of dilation. *J. Am. Coll. Cardiol.* 16:569–575, 1990.
[24]Holzapfel, G. A. Nonlinear Solid Mechanics. A Continuum Approach for Engineering. John Wiley & Sons, Chichester, 2000.
[25]Holzapfel, G. A., and T. C. Gasser. A viscoelastic model for fiber-reinforced composites at finite strains: Continuum basis, computational aspects and applications. *Comput. Methods Appl. Mech. Eng.* 190:4379–4403, 2001.
[26]Holzapfel, G. A. and T. C. Gasser. Computational stress–deformation analysis of arterial walls including high-pressure response. *Int. J. Cardiol.* 116:78–85, 2007.
[27]Holzapfel, G. A., T. C. Gasser, and R. W. Ogden. A new constitutive framework for arterial wall mechanics and a comparative study of material models. *J. Elasticity* 61:1–48, 2000.
[28]Holzapfel, G. A., T. C. Gasser, and R. W. Ogden. Comparison of a multi-layer structural model for arterial walls with a Fung-type model, and issues of material stability. *J. Biomech. Eng.* 126:264–275, 2004.
[29]Holzapfel, & Ogden (Eds) Biomechanics of Soft Tissue in Cardiovascular Systems. Springer-Verlag, Wien – New York, 2003.
[30]Holzapfel, G. A., C. A. J. Schulze-Bauer, and M. Stadler. Mechanics of angioplasty: Wall, balloon and stent. In Casey, J. and G. Bao (eds.) Mechanics in Biology. New York: The American Society of Mechanical Engineers (ASME). AMD-Vol. 242/BED-Vol. 46, 2000, pp. 141–156.
[31]Holzapfel, G. A., G. Sommer, M. Auer, P. Regitnig, and R. W. Ogden. Layer-specific 3D residual deformations of human aortas with non-atherosclerotic intimal thickening. *Ann. Biomed. Eng.*, doi 10.1007/s10439-006-9252-z, in press.
[32]Holzapfel, G. A., G. Sommer, and P. Regitnig. Anisotropic mechanical properties of tissue components in human atherosclerotic plaques. *J. Biomech. Eng.* 126:657–665, 2004.
[33]Holzapfel, G. A., M. Stadler, and T. C. Gasser. Changes in the mechanical environment of stenotic arteries during interaction with stents: Computational assessment of parametric stent design. *J. Biomech. Eng.* 127:166–180, 2005.
[34]Holzapfel, G. A., M. Stadler, and C. A. J. Schulze-Bauer. A layer-specific three-dimensional model for the simulation of balloon angioplasty using magnetic resonance imaging and mechanical testing. *Ann. Biomed. Eng.* 30:753–767, 2002.
[35]Holzapfel, G. A. and H. W. Weizsäcker. Biomechanical behavior of the arterial wall and its numerical characterization. *Comp. Biol. Med.* 28:377–392, 1998.
[36]Huber, M. S., J. F. Mooney, J. Madison, and M. R. Mooney. Use of a morphologic classification to predict clinical outcome after dissection from coronary angioplasty. *Am. J. Cardiol.* 68:467–471, 1991.
[37]Humphrey, J. D. Cardiovascular Solid Mechanics. Cells. Tissues, and Organs. Springer-Verlag, New York, 2002.

[38]Jain, S. P., A. Jain, T. J. Collins, S. R. Ramee, and C. J. White. Predictors of restenosis: A morphometric and quantitative evaluation by intravascular ultrasound. *Am. Heart J.* 128:664–673, 1994.
[39]Kachanov, L. M. Introduction to Continuum Damage Mechanics. Martinus Nijhoff Publishers. Dordrecht, The Netherlands, 1986.
[40]Lendon, C. L., M. J. Davies, G. V. R. Born, and P. D. Richardson. Atherosclerotic plaque caps are locally weakened when macrophages density is increased. *Atherosclerosis* 87:87–90, 1991.
[41]Losordo, D. W., K. Rosenfield, A. Pieczek, K. Baker, M. Harding, and J. M. Isner. How does angioplasty work? Serial analysis of human iliac arteries using intravascular ultrasound. *Circulation* 86:1845–1858, 1992.
[42]MacLean, N. F., N. L. Dudek, and M. R. Roach. The role of radial elastic properties in the development of aortic dissections. *J. Vasc. Surg.* 29:703–710, 1999.
[43]Ogden, R. W. Non-linear Elastic Deformations. Dover, New York, 1997.
[44]Oliver, J. Modelling strong discontinuities in solid mechanics via strain softening constitutive equations Part 1: Fundamentals. *Int. J. Numer. Methods Eng.* 39:3575–3600, 1996.
[45]Ortiz, M. and A. Pandolfi. Finite-deformation irreversible cohesive elements for three-dimensional crack-propagation analysis. *Int. J. Numer. Methods Eng.* 44:1267–1282, 1999.
[46]Patel, D. J., J. S. Janicki, and T. E. Carew. Static anisotropic elastic properties of the aorta in living dogs. *Circ. Res.* 25:765–779, 1969.
[47]Popma, J. J., M. B. Leon, G. S. Mintz, K. M. Kent, L. F. Satler, T. J. Garrand, and A. D. Pichard. Results of coronary angioplasty using the transluminal extraction catheter. *Am. J. Cardiol.* 70:1526–1532, 1992.
[48]Purslow, P. P. Positional variations in fracture toughness, stiffness and strength of descending thoracic pig aorta. *J. Biomech.* 16:947–953, 1983.
[49]Rhodin, J. A. G. Architecture of the vessel wall. In Bohr, D. F. A. D. Somlyo, & H. V. Sparks (eds.) Handbook of Physiology, The Cardiovascular System. 2 American Physiological Society, Bethesda, Maryland: 1–31, 1980.
[50]Richardson, P. D.. Biomechanics of plaque rupture: Progress, problems, and new frontiers. *Ann. Biomed. Eng.* 30:524–536, 2002.
[51]Richardson, P. D. Mechanical properties of atherosclerotic tissues. In Holzapfel, G. A. & R. W. Ogden (eds.) Mechanics of Biological Tissue. Springer-Verlag, Heidelberg: 207–223, 2006.
[52]Roach, M. R., J. C. He, and R. G. Kratky. Tear propagation in isolated, pressurized porcine thoracic aortas. *Can. J. Cardiol.* 15:569–575, 1999.
[53]Rose, J. H., J. Ferrante, and J. R. Smith. Universal binding energy curves for metals and bimetallic interfaces. *Phys. Rev. Lett.* 47:675–678, 1981.
[54]Rose, J. H., J. R. Smith, and J. Ferrante. Universal features of bonding in metals. *Phys. Rev. B* 28:1835–1845, 1983.
[55]Saber, R. S., W. D. Edwards, K. R. Bailey, T. W. McGovern, R. S. Schwartz, and D. R. Holmes Jr. Coronary embolization after balloon angioplasty or thrombolytic therapy: An autopsy study of 32 cases. *J. Am. Coll. Cardiol.* 22:1283–1288, 1993.
[56]Salunke, N. V. and L. D. T. Topoleski. Biomechanics of atherosclerotic plaque. *Crit. Rev. Biomed. Eng.* 25:243–285, 1997.
[57]Schöberl, J. NETGEN – A 3D Tetrahedral Mesh Generator – Version 4.2. University Linz, Austria, 2002.
[58]Sommer G., T. C. Gasser, P. Regitnig, M. Auer, and G. A. Holzapfel. Dissection of the human aortic media: An experimental study. *J. Biomech. Eng.*, in press.
[59]Stary, H. C. Atlas of Atherosclerosis: Progression and Regression (2nd ed.). The Parthenon Publishing Group Limited. Boca Raton London, New York, Washington, D.C., 2003
[60]Taylor, R. L. FEAP – A Finite Element Analysis Program. Version 7.4 User Manual. University of California at Berkeley, Berkeley, California, 2002.
[61]Tobis, J. M., J. Mallery, D. Mahon, K. Lehmann, P. Zalesky, J. Griffith, J. Gessert, M. Moriuchi, M. McRae, and M. L. Dwyer, et al.. Intravascular ultrasound imaging of human coronary arteries in vivo. Analysis of tissue characterizations with comparison to in vitro histological specimens. *Circulation* 83:913–926, 1991.
[62]Toussaint, J. F., J. F. Southern, V. Fuster, and H. L. Kantor. Water diffusion properties of human atherosclerosis and thrombosis measured by pulse field gradient nuclear magnetic resonance. *Arterioscler. Thromb. Vasc. Biol.* 17:542–546, 1997.
[63]Toussaint, J. F., J. F. Southern, H. L. Kantor, I. K. Jang, and V. Fuster. Behavior of atherosclerotic plaque components after in vitro angioplasty and atherectomy studied by high field MR imaging. *Magn. Reson. Imaging* 16:175–183, 1998.
[64]Weizsäcker, H. W. and J. G. Pinto. Isotropy and anisotropy of the arterial wall. *J. Biomech.* 21:477–487, 1988.
[65]Wolinsky, H. and S. Glagov. A lamellar unit of aortic medial structure and function in mammals. *Circ. Res.* 20:90–111, 1967.
[66]Wriggers, P. Computational Contact Mechanics. John Wiley & Sons, Chichester, 2002.
[67]Zhou, J. and Y. C. Fung. The degree of nonlinearity and anisotropy of blood vessel elasticity. *Proc. Natl. Acad. Sci. USA* 94:14255–14260, 1997.